Proposal of a new design of source heat exchanger for the technical feasibility of solar thermal plants coupled to supercritical power cycles

María José Montes [a,*], José Ignacio Linares [b], Rubén Barbero [a], Antonio Rovira [a]

[a] E.T.S. Ingenieros Industriales - UNED, C/Juan del Rosal 12, 28040 Madrid, Spain
[b] Rafael Mariño Chair in New Energy Technologies – COMILLAS-ICAI, C/Alberto Aguilera 25, 28015 Madrid, Spain

ARTICLE INFO

ABSTRACT

Solar thermal power plants coupled to supercritical CO_2 cycles seems to be a way to increase the global solar-to-electric efficiency. For that, the concentrating solar technology that is best integrated is the molten salt central receiver with a thermal energy storage associated. This work is focused on one of the main challenges of this scheme: the source heat exchanger transferring the thermal energy from the molten salt in the solar field to the CO_2 in the power cycle. A new design, based on the printed circuit heat exchanger technology is proposed, that withstands the pressure difference and avoids the molten salt plugging when circulating through microchannels. The thermo-mechanic model of this heat exchanger is also calculated.

This work also addresses a thermo-economic optimization of the printed circuit heat exchanger proposed. For that, it is considered the global performance of the solar thermal plant for three layouts: recompression, inter-cooling and partial-cooling cycles. This optimization yields to a great reduction in the investment cost of these source heat exchangers, achieving the lowest cost in the partial-cooling configuration, followed by the inter-cooling and finally, the recompression. This trend is also observed in the global performance of the solar plant, so the partial-cooling layout is the one with the lowest levelized cost of electricity; this value is similar to that of the intercooling layout, and both are well below from the cost in the recompression layout, which results the most expensive configuration.

1. Introduction

The future competitiveness of concentrating solar thermal energy, compared to other renewable energies, is conditioned by a decrease in the cost of the final energy produced. For this purpose, two research approaches have emerged within the concentrating solar energy. The first attempts to minimize investment costs at the expense of a decrease in overall efficiency; this approach has found an important market niche in the supply of process heat to the industry at medium temperature. The second approach has focused on increasing thermal performance, working with higher concentration ratio and temperature, even if this means significantly increasing investment costs. For this purpose, one of the most promising schemes consists of the integration between super-critical CO_2 (sCO_2) Brayton cycles and central receiver (CR) systems working with a heat transfer fluid (HTF) at high temperature (Mehos et al., 2017): molten salt, liquid metal, falling particles or a gas-phase fluid. This work has focused on the molten salt (MS), with a thermal energy storage (TES) associated, because this scheme has a high capacity

factor and presents the advantages of reliability and dispatchability in the electricity production. One of the main technological challenges of this solar thermal power plant (STPP) is the heat exchanger to transfer the thermal energy from the MS in the solar field to the sCO_2 in the power cycle: the source heat exchanger (SHX). This work deals in more depth with this last point, proposing a design of molten salt-to-sCO_2 heat exchanger (HX) that seeks to address some of the technological issues arising for this type of HXs, such as: the mechanical stress produced by the pressure difference; the corrosion associated to working with salts at high temperature; and the possibly plugging of the salt when circulating through microchannels, as it will be explained later.

1.1. Supercritical CO_2 Brayton cycles

According to Wang et al. (2017), sCO_2 cycles have a very high efficiency, above 50%, even with dry cooling; compared to conventional water-steam Rankine cycles, these supercritical cycles exhibit several technological advantages, i.e.: sCO_2 is less corrosive than steam, so its handling at high temperature is easier; the operation beyond the critical

---

Acronyms

AC	Auxiliary Compressor
ASME	American Society of Mechanical Engineers
CR	Central Receiver
CHX	Compact Heat Exchanger
FPHE	Formed Plate Heat Exchanger
HTF	Heat Transfer Fluid
HTR	High Temperature Recuperator
HX	Heat Exchanger
HXE	Heat Exchanger Element
H^2X	Hybrid Heat Exchanger
LCOE	Levelized Cost of Electricity
LTR	Low Temperature Recuperator
MC	Main Compressor
MS	Molten Salt
PC	Pre-Cooler
PCHE	Printed Circuit Heat Exchanger
STPP	Solar Thermal Power Plant
SHX	Source Heat Exchanger
T	Turbine
TES	Thermal Energy Storage
TM	Turbomachines
IC	Intercooler
HTP	High Temperature Pump
LTP	Low Temperature Pump
SIR	Savings-to-Investment Ratio
CRF	Capital-Recovery Factor
CELF	Constant-Escalation Levelization Factor

Latin letters

A	Area
c	Specific heat
C	Cost
CM	Cost factor of material
C_E	Electricity cost
D_h	Hydraulic diameter
d	Diameter
dP	Pressure Drop
f	Darcy/Fanning pressure friction loss factor
h	Enthalpy
h_{conv}	Convection heat transfer coefficient
i_{eff}	Effective discount rate

k	Thermal conductivity
L_c	Characteristic length
L	Length
M	Mass
$\dot{m}$	Mass flow rate
N	Number of channels/elements
n	Number of years
Nu	Nusselt number
p	Pressure
Pr	Prandtl number
$\dot{Q}$	Thermal power
r_n	Nominal escalation rate
Re	Reynolds number
T	Temperature
TA	Temperature Approach
U	Overall heat transfer coefficient
u	Velocity
V	Volume
Y	Yearly operation time
Zw	Angle between the z-axis and the normal vector to the surface

Greek Letters

η	Cycle/receiver efficiency
ρ	Density
μ	Dynamic viscosity
σ	Ratio of free flow area to frontal area

Subscripts

0	Base case
amb	Ambient
ave	Average
conv	Convection
f	Fluid
i	i-th element
j	j-th element
loss	Heat loss
net	Net
p	Pressure
r	Infrared (super-index)
rad	Radiation
s	Solar (super-index)
th	Thermal

point (7.38 MPa, 31 °C), but not far, yields to a smaller size of the turbomachinery, as well as a decrease in the compression power.

These cycles support both direct and indirect integration; because sCO_2 receivers are not yet developed, in the short term it is more likely the indirect integration, using the state-of-art technology of molten salt receiver and thermal storage (Mehos et al., 2017). So, the possible supercritical cycles that can be indirectly coupled to a CR are analysed according to different parameters, highlighting: the cycle efficiency; the complexity of the cycle, in terms of additional components compared to the most common one, the recompression cycle; and the temperature difference of the sCO_2 in the source heat exchanger (SHX), which determines the temperature difference in the molten salts and therefore the investment in the coupled solar subsystem (Crespi et al., 2017; Wang et al., 2017).

For a hot salt temperature between 600 °C and 800 °C, the cycle with higher efficiency is the intercooling cycle, followed by the recompression layout. The recompression cycle is the less complex, with only an extra compressor added, while the intercooling and the partial-cooling cycles are the most complex, as they need of two extra

compressors and an extra inter-cooler. Regarding the SHX temperature difference, the partial-cooling cycle presents the largest temperature difference (Crespi et al., 2017; Wang et al., 2017). In summary, there is not any cycle with a clear advantage over the others; the choice of one or the other should be based on an annual analysis of the global plant, and it will depend on the specific operating and ambient conditions.

A later work of NREL (Neises and Turchi, 2019) analyses the global performance of two STPPs based on the recompression and partial-cooling sCO_2 cycles. They find the important conclusion that, although the recompression cycle has a higher efficiency and is less complex than the partial-cooling cycle, the STPP with partial-cooling presents lower investment cost and generates more net electricity; this is due to the larger temperature difference in the main heat input for the partial-cooling layout, that yields to smaller storage tanks, higher receiver efficiencies and lower pump consumption, as the molten salt flow rate is also lower.

Following that research line, this work analyses the design and the thermal economic optimization of a MS-to-CO_2 SHX, integrated in three different STPPs, coupled to three different supercritical layouts:

Table 1
Thermal properties of the ternary chloride salt MgCl$_2$/NaCl/KCl.

Thermal property	Correlation
Specific heat (J/kg/°C)	$c_p = 1180$
Density (kg/m^3)	$\rho = 1899.3 - 0.43 \cdot T$ (°C)
Thermal conductivity (W/m/°C)	$k = 0.5423 - 0.0002 \cdot T$ (°C)
Dynamic viscosity (Pa·s)	$\mu = 8.25 \cdot 10^{-6} \cdot \exp(11874.71735/1350.84595 + T(°C))$

Source: Linares et al., 2020.

Fig. 1. Conventional printed circuit heat exchanger.

recompression, intercooling and partial-cooling cycles. Compared to the previous study of NREL, the intercooling cycle has been also introduced as a possible candidate to minimize the cost of the electricity production. The partial-cooling and intercooling cycles differ from the simple recompressed cycle in that the main compressor is divided into two main compressors with an intercoling between them. The difference between the intercooling and the partial-cooling layouts are the different inlet conditions to the auxiliar compressor. This different configuration yields to larger temperature increment of the sCO$_2$ in the SHX of the partial-cooling cycle, which is advisable for the STPP since it reduces the required molten salt volume. On the other hand, the intercooling layout achieves a decrease in the compression work that yields to a higher thermal efficiency than the recompression and partial-cooling cycles.

1.2. Power towers working with molten salts at high temperature

The state-of-art molten salt used in CR systems with TES is the nitrate solar salt. The main drawback of this salt is its thermal decomposition temperature, in the range of 600 °C, which is far from the target temperatures required by efficient supercritical cycles, greater than or equal to 700 °C. So, other alternative salts, with thermal stability about 750 °C, are proposed and studied (Turchi et al., 2018). These candidate salts consist of binary and ternary chloride and carbonate salt blends. Although it is difficult to decide that one molten salt is better than another, and more effort is required to perform high temperature corrosion studies for a prolonged exposure of time, the ternary chloride salt MgCl$_2$/NaCl/KCl has been selected for this study. This salt exhibits the following advantages: a low melting point and a high thermal decomposition temperature, yielding to a large working temperature range; a volumetric heat capacity above those of other chloride salts; and the cheapest estimated cost. Table 1 summarizes the main thermal properties of the ternary chloride molten salt selected (Linares et al., 2020).

The central receiver is a tubular cavity-type, as the working temperatures are higher than those in conventional STPPs based on external MS receivers (Mehos et al., 2017). The cavity configuration is recommended for high temperatures (Turchi et al., 2018), because the radiation heat loss is lower compared to external receivers working at the same temperatures.

1.3. The heat exchanger between the solar field and the supercritical power cycle

This last section of the introduction is dedicated to the MS-to-sCO$_2$ heat exchanger that transfers the thermal energy between the solar field and the supercritical power block. As a simple proposal, the shell-and-tube heat exchanger could be proper for this layout, with the sCO$_2$ circulating inside the tubes and the MS through the shell. However, due to the high pressures of the sCO$_2$, the increase in the tubes thickness can lead to a limited performance of these HXs.

An advanced heat exchanger design is key for both the economic and performance viability of STPPs coupled to supercritical power cycles. The most promising proposals include compact heat exchangers (CHX) and, particularly, printed circuit heat exchangers (PCHE). PCHE consists
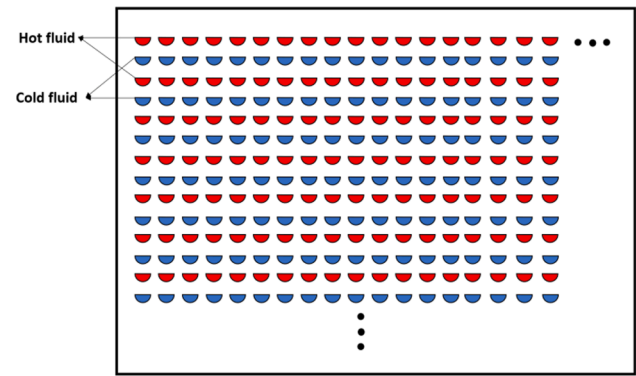
of chemically etched plate sheets joined by diffusion, alternating hot-cold rows of semi-circular channels, as seen in Fig. 1. The major manufacturer of PCHEs is Heatric, Inc. (2020). In general, the flow channels of the PCHE may be divided into four types (Fu et al., 2019): straight, zig-zag, S-shaped and airfol; although the last three increase the PCHE thermal-hydraulic performance, friction loss and MS plugging risk are also increased, so this study has been limited to straight channels.

Within the PCHEs, three types can be distinguished (Southall et al., 2008): conventional PCHE; Formed Plate Heat Exchangers (FPHEs), in which layers consist of fins, bounded by side bars and separated by flat parting sheets; and Hybrid Heat Exchangers (H^{2}Xs), which are a combination of both, PCHE and FPHE. Due to the small diameter of the channels in these HXs, they can withstand high pressures but, as the channel diameter is increased, the design pressure decreases. Then, FPHEs and H^{2}Xs are suitable for working at lower pressures than PCHEs. As the higher working pressures in the three supercritical cycles selected range from 210 bar to 250 bar, whereas the working temperature is near to 700 °C, the proper HX is the PCHE, so the characteristics of this type are deeply studied below.

PCHEs have been widely studied by the nuclear research, being recommended for sCO$_2$ power cycles (Dostal, 2004). The microchannels are well suited to the supercritical fluid, since they withstand high pressures and enhance heat transfer because of the convection coefficient and the hydraulic diameter are inversely related. So, these heat exchangers meet the main requirements of high-pressure heat transfer, and there are many designs proposed for sCO$_2$-to-sCO$_2$, as the recuperators in closed supercritical cycles (Shiferaw and Carrero, 2016).

However, when the heat exchange is MS-to-sCO$_2$, new concerns arise from the possible clogging of the viscous liquid phase, with relatively low Reynolds numbers, in the microchannels designed to optimize heat transfer of the supercritical phase. This problem has been reported in several studies of both nuclear (INPRO, 2013) and solar power plants (Iverson et al., 2013), since in both cases it has been considered the coupling of the thermal source to sCO$_2$ power cycles, as well as the use of molten salts or liquid metals as the heat transfer and the thermal storage fluid. As said in (Iverson et al., 2013), this problem is mitigated by the working conditions of this primary heat exchanger in recuperated supercritical Brayton cycles, in which the temperature of the external source ranges from 500 °C to 700 °C, approximately.

The proposal of a MS-to-sCO$_2$ heat exchanger, operating in the required conditions and overcoming the issue described above, is a mandatory challenge for the development of the supercritical STPP technology. Despite this, very few designs, proposed in the literature, address this problem. The most recent studies have focused on trying to improve the heat transfer by means of the use of airfoil fins in the microchannels (Fu et al., 2019). However, it seems that the heat transfer enhancement is limited and instead, the maximum allowable pressure is reduced to 200 bar, which does not make them suitable for these applications. On the other hand, a study (Sun et al., 2018a,b) has been
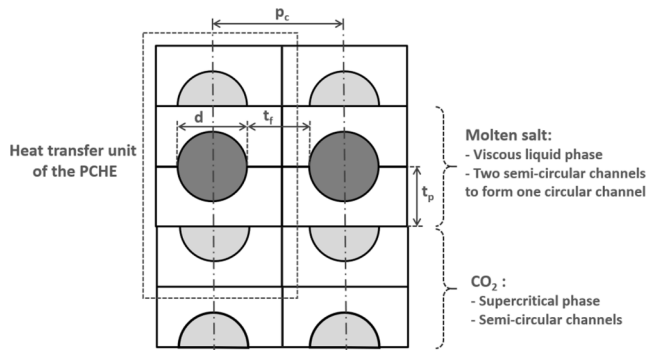
Fig. 2. Heat transfer unit of the PCHE proposed and main parameters. (d = channel diameter; p_c = channel pitch; t_f = thickness between channels t_p = plate thickness).

Table 2
Basic geometric parameters of the PCHE (Source: Heatric, Inc. 2020, and own calculations).

Channel diameter (d, mm) (recommended [6])	2
Channel pitch (p_c = 1.1·d, mm)	2.2
Thickness between channels (t_f = p-d, mm)	0.2
Plate thickness (t_p, calculated, mm)	2.1

found that addresses the problem of the molten salt plugging in microchannels, proposing a PCHE design between a molten salt cooled nuclear reactor and a supercritical Brayton cycle. The basic principle of this design is to face two etched plates intended for molten salt, so that a circular channel is formed for salt, maintaining the semi-circular channel for sCO$_2$, as shown in the Fig. 2. Besides that, straight channels are selected. It is obvious that this design does not optimize the heat transfer, but this is not a priority as the thermal conductivity of the molten salt is relatively large. Instead, the plugging and the corrosion problems are mitigated, as the cross-section area is greater and the contact area is reduced.

This new design is studied in this paper, for the coupling between the CR and the sCO$_2$ cycles, adapting the PCHE to the working conditions of each of the three proposed layouts: recompression, intercooling and partial-cooling. The Section 2 of this paper describes the development of the thermal and mechanical model of the PCHE. The Section 3 is focused on the solar field and the Brayton cycles models, as it is necessary to simulate the heat exchanger in a suitable framework. The fourth and last section shows the thermo-economic optimization of the PCHE. Regarding other optimizations that estimate the operation cost by means of the pumping power through the PCHE (Yoon et al., 2014; Sun et al., 2018ab), the analysis accomplished in this paper is based on a more global definition of the operation cost, accounting for the global STPP performance.

2. Thermo-mechanic model of the new design of PCHE

As said in the introduction, the first part of this work is focused on the mechanical and thermal design of the PCHE proposed, Fig. 2.

There are several geometrical parameters that must be defined prior of the thermo-fluid dynamic simulation. The channel diameter, the channel pitch and the thickness between channels has been set according to Heatric, Inc. (2020) recommendations and they are shown in Table 2.

Although there is also a recommended value for the thin wall thickness, a mechanical calculation has been made for this value, as it is identified as a critical thickness to withstand the design pressure at the design temperature. The design method was provided by Heatric for diffusion-bonded microchannel heat exchangers (Le Pierres et al., 2011) and is a simplified model originating from the design requirements for non-circular vessels with rectangular cross-section supported by stayed plates in ASME codes (2010). Following the recommendations of this method, the plate thickness is calculated to be 2.1 mm, as shown in Table 2. The withstanding to the working conditions is addressed in thermo-mechanical stress studies, for general PCHEs, accomplished by (Heatric, Inc., 2020), concluding that this type of HXs can work at 250 bar and 700 °C.

Regarding the material of the PCHE, a first study (Dewson and Li, 2005) pointed out that the alloy selected must withstand high temperatures and pressures; it must also be available in sheet and plate form, which are the most compatible forms with the manufacture of this HX. In a later study about advanced HXs for molten salts (Sabharwall et al., 2014), it is highlighted that the material used must show a good corrosion resistance in MS at temperatures up to 700 °C. In this study, two nickel-molybdenum-chromium alloys are selected: Hastelloy N and Haynes 242. Table 3 shows the composition and the main characteristics of both alloys.

The material finally selected is Haynes 242, because: its resistance to corrosion of ternary chloride molten salts is greater due to the higher percentage of molybdenum (Sun et al., 2018a,b); and, overall, the maximum allowable stress at the design temperature is higher than that of Hastelloy N. These two characteristics, together with the non-irradiated working conditions of this HXs, make the Haynes 242 the best material for the new design of PCHE.

2.1. Thermo-fluid dynamic model of the PCHE

The thermal power, as well as the inlet temperatures of both chloride MS and sCO$_2$ are inputs to the thermal model of the PCHE, as they are fixed by the cycle or the solar receiver. Besides that, all the geometrical parameters of the thermal unit represented in Fig. 2 are also inputs to the model. There are two other inputs that must be defined for the designer: the temperature approach (TA$_{MS-sCO2}$) between both streams and the pressure drop of the supercritical phase (dP$_{sCO2}$). Both variables affect the size of the heat exchanger, and therefore, its cost. As it will be explained in Section 4, these two inputs will be taken as the basis for the parametric design optimization study. Once the TA$_{MS-sCO2}$ is set, the two outlet temperatures are also fixed, as the PCHE is considered to be a balanced counter-flow heat exchanger; on the other hand, once the pressure drop of the supercritical phase is set, the velocity of both streams, as well as the cross flow area (the same for both streams) is fixed, by means of an iterative process based on an initial value of sCO$_2$ velocity. Finally, the MS pressure drop is also fixed to a value much lower than the sCO$_2$ pressure drop.

The basic equations describing the model are summarized in the Appendix A. It is important to point out that those equations have been

Table 3
Candidate materials for the PCHE proposed.

Material	Composition (% weight)	Salt corrosion resistance	Air corrosion resistance	Irradiation resistance	Metallurgical stability
Hastelloy N	71% Ni − 7% Cr − 16% Mo	Excellent	Good	Good	Good
Haynes 242	65%Ni − 8% Cr − 25% Mo	Very good	Good	Adequate	Good

Table 4

Main thermal characteristics of the base and optimized configuration of the PCHE simulated, for each supercritical layout.

PCHE	Recompression		Intercooling		Partial-cooling	
	Base case	Optimized	Base case	Optimized	Base case	Optimized
Sizing and geometrical characteristics						
Frontal area (m^2)	11.375	6.568	8.634	3.784	8.377	3.504
Lenght (m)	4.816	2.028	6.123	3.198	6.824	3.195
Height (m)	18.958	10.946	14.390	6.306	13.961	5.840
Width (m)	0.6	0.6	0.6	0.6	0.6	0.6
Volume (m^3)	54.777	13.320	52.868	12.102	57.161	11.197
Number of modules	128	38	120	33	120	30
Heat transfer area (m^2)	19078.41	4639.200	18413.339	4214.950	19908.560	3899.662
Number of channels (MS)	630,540	364,063	478,588	209,749	464,340	194,227
Number of channels (sCO$_2$)	1,261,080	728,126	957,176	419,498	928,680	388,454
Material	Haynes-242					
Thermal characteristics						
Thermal power (MWth)	100.992	100.992	97.402	97.402	103.419	103.419
U$_{average}$ (W/m^2/°C)	542.577	626.172	545.683	665.568	540.134	668.616
Primary (Chloride molten salt)						
Maximum velocity (m/s)	0.190	0.334	0.191	0.442	0.183	0.446
Inlet temperature (°C)	700	700	700	700	700	700
Inlet pressure (bar)	6	6	6	6	6	6
Mass flow rate (kg/s)	600.185	610.895	457.815	465.824	426.488	434.738
Outlet temperature (°C)	557.4	559.9	519.7	522.8	494.5	498.4
Outlet pressure (bar)	5.940	5.956	5.919	5.902	5.909	5.897
Pressure drop (bar)	0.060	0.044	0.081	0.098	0.091	0.103
h$_{conv}$ (W/m^2/°C)	908.851	908.305	917.076	916.400	922.574	921.723
Secondary (sCO2)						
Maximum velocity (m/s)	2.709	4.663	2.190	4.959	2.106	4.977
Inlet temperature (°C)	690	665	690	665	690	660
Inlet pressure (bar)	200	200	250	250	250	250
Mass flow rate (kg/s)	565.054	577.080	428.124	436.635	399.329	408.132
Outlet temperature (°C)	547.399	524.899	509.699	487.799	484.499	458.398
Outlet pressure (bar)	200.495	200.493	250.494	250.991	250.485	250.982
Pressure drop (bar)	0.495	0.493	0.494	0.991	0.485	0.982
h$_{conv}$ (W/m^2/°C)	1471.858	2310.508	1473.692	2874.373	1421.100	2879.948
Costs						
Inversion Cost (Mio.$)	38.769	9.427	37.417	8.565	40.456	7.924

Table 5

Numerical results from CFD vs data calculated by analytical model.

	Numerical	Analytical
Outlet sCO$_2$ temperature (°C)	655.28	660
Outlet MS temperature (°C)	491.1	498.4
Pressure drop for sCO$_2$ (bar)	1.076	0.98
Pressure drop for MS (bar)	0.1026	0.048

already used in other thermal models of PCHE (Dostal, 2004; Ariu, 2014; Yoon et al., 2014). Nevertheless, a numerical validation of the model will be accomplished in next section. To conclude this section, Table 4 shows the sizing, geometrical and thermal parameters for two PCHE configurations of each of the three supercritical layouts considered (recompression, intercooling and partial-cooling). These two configurations are the base configuration and the optimized configuration, calculated by the thermo-economic method explained in Section 4. The TA$_{MS-sCO2}$ between both streams and the dP$_{sCO2}$ are fixed to 10 °C and 0.5 bar, respectively, for the base case of the three layouts. In the optimized case, these parameters have different values, calculated by the optimization process. These values are also shown in Table 10, as a result of the optimization method.

2.2. Numerical validation of the PCHE analytical model

The validation of the two-dimensional analytical model has been carried out by means of a numerical model in CFD, of one of the heat
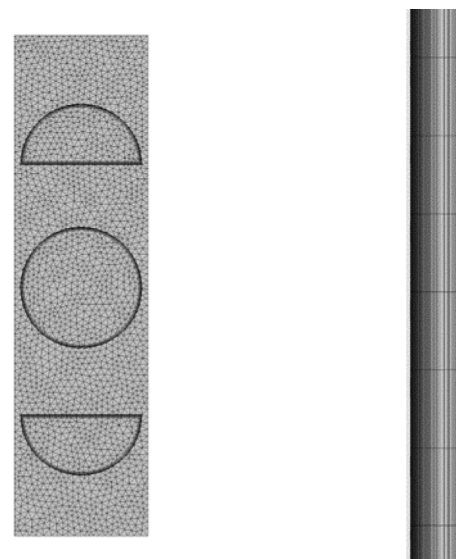
Fig. 3. Transversal and longitudinal sections of the 3D model.

exchangers shown in Table 4; in particular, the PCHE obtained for the partial-cooling configuration. To simplify the problem, a continuous length of the heat exchanger is assumed, without inlet/outlet arrangements between modules, as the longitudinal heat transfer is negligible. In this way, the problem becomes a pure counterflow heat transfer problem. The simulation is carried out using ANSYS CFX code.
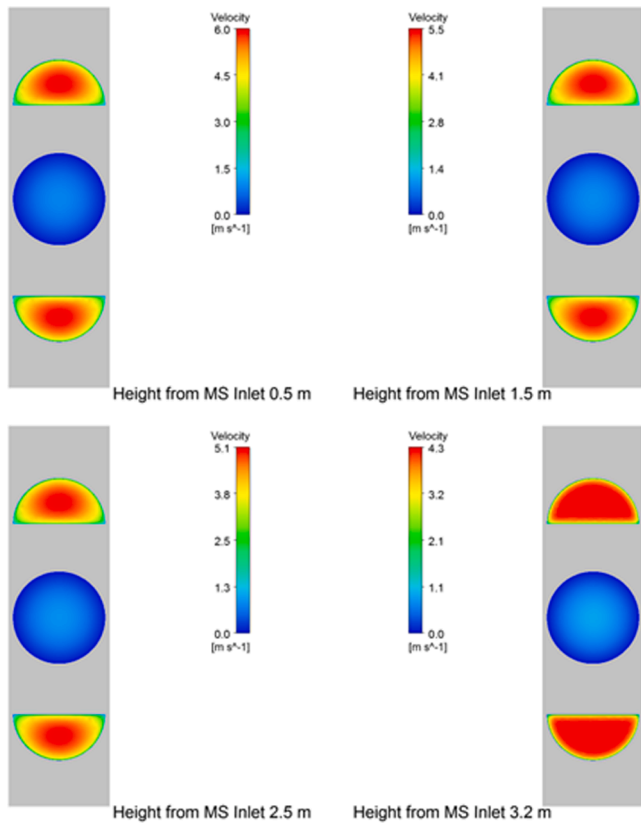
Fig. 4. Velocity distribution (front view) for the molten salt and the sCO$_2$ at 0.5 m, 1.5 m, 2.5 m and 3.2 m from the molten salt inlet.
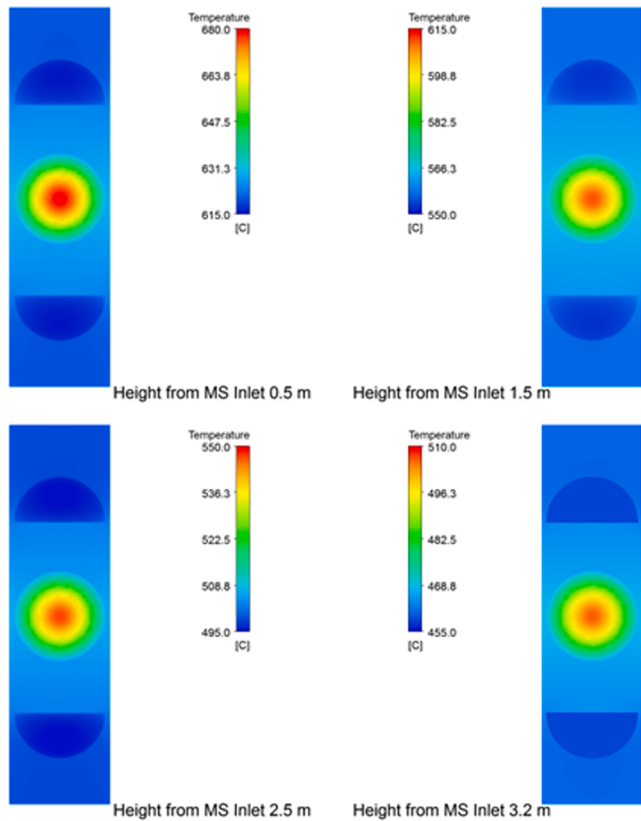
Fig. 5. Temperature distribution (front view) for the molten salt, the sCO$_2$ and the solid at 0.5 m, 1.5 m, 2.5 m and 3.2 m from the molten salt inlet.

The simulated 3D model includes a basic section that repeated in a plane form the complete heat exchanger, so symmetry/adiabatic conditions can be applied as side boundary conditions. Inlet temperatures and mass flows for both fluids are taken from Table 4 as boundary conditions in the model. The mesh (Fig. 3) is obtained by extrusion of a surface mesh at the molten salt inlet plane in order to save mesh elements. A prism layer is also implemented at the walls, within the fluid sides, in order to model the boundary layer adequately. A sensitivity analysis is performed to avoid influence of mesh refinement in results. The final mesh used is composed of 3,348,992 of nodes or 5,058,730 of elements (tetrahedrons, prisms and hexahedrons).

As said in the thermal model description (Appendix A), the flow regime is laminar for the chloride MS, and turbulent for the sCO$_2$. Each regime is simulated separately using the suitable model, as the heat transfer and the fluid-dynamic mechanisms are different for the laminar and the turbulent flow. In the case of turbulent flow the Shear Stress Transport (SST) model (ANSYS, 2020) is used, which uses a standard k-ε for the bulk and a k-ω in the boundary layer. Prism layer is adapted to the required size (in this case, Y$^+$ for the nearest node below 1, which corresponds with the non-dimensional distance to the wall).

The thermo-physical properties of the chloride MS are directly introduced in the model using polynomials in terms of temperatures shown in Table 1. In the case of the sCO$_2$, the thermodynamic properties have been tabulated from NIST database (2020) in the working region of the PCHE, for temperature steps below 0.4 °C and pressure steps equal to 0.05 bar. Figs. 4 and 5 show the velocity and temperature distributions, respectively, at some different heights from the molten salt inlet section.

Table 5 shows the numerical results obtained from the CFD model compared to the data from the analytical model. The maximum deviation between the numerical temperature and that obtained from Gnielinski correlation is 3.6%, which is within the range of confidence reported for Gnielinski correlation (Srivastava et al., 2013). The pressure drop for the sCO$_2$ is very similar, so Techo correlation seems to be adequate to estimate the supercritical phase friction loss through semicircular channels. Finally, a higher relative error is observed in calculating the friction loss of the molten salt in laminar regime. This is probably because the low Reynolds numbers of the laminar and viscous molten salt flow are difficult to capture by the numerical model, and more effort is needed in this line. Nevertheless, there are several references (Srivastava et al., 2013) that shows a good agreement between numerical results and analytical data calculated from Poiseulle's equation. These references, as well as the small value of this friction loss, make this error negligible, so it is considered that the model is validated.

3. Thermal model of the solar thermal plant

The thermal-economic optimization of the PCHE described in the previous section requires an adequate framework of comparison, which accounts for the changes in the overall plant performance, caused by the different designs of this heat exchanger. A simplified scheme of the global solar thermal power plant coupled to the supercirtical cycle is shown in Fig. 6.

In the next section it is explained the energy models of the main components of the two subsystems coupled by the source heat exchanger: the solar field, employing the ternary MS as HTF, and the supercritical cycles based on sCO$_2$.

3.1. Supercritical cycle layouts

As said in the introduction, three different supercritical layouts have been selected: the recompression, the intercooling and the partial-cooling cycles. The cycle power output has been set at 50 MW$_e$, as Khi Solar One plant, which is the largest STPP based on cavity receiver and currently in commercial operation (SolarPACES, 2020). These three supercritical layouts are showed in Figs. 7a, 7b and 7c, respectively.

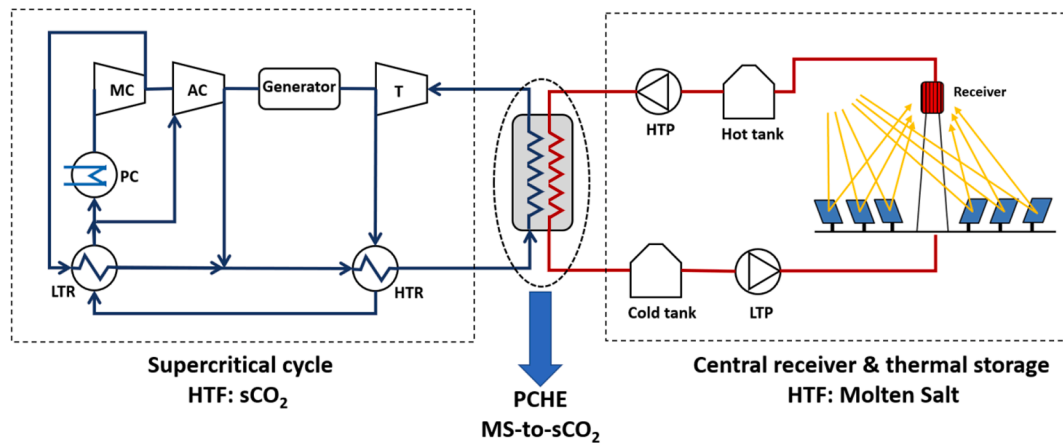The three cycles are based in the recompression configuration, so

Fig. 6. Scheme of the complete supercritical solar thermal power plant with the source heat exchanger (PCHE) between the solar field and the power cycle.
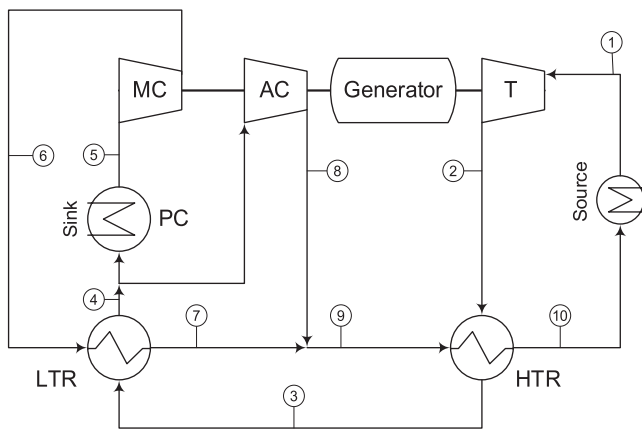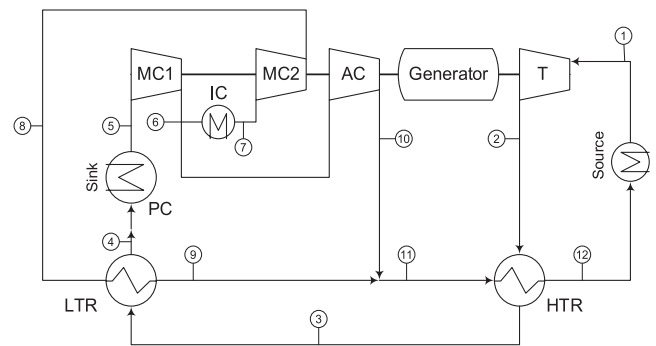

Fig. 7a. Recompression cycle layout.
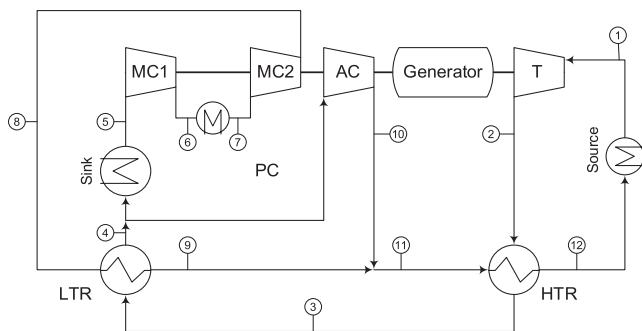

Fig. 7c. Partial-cooling cycle layout.

Fig. 7b. Intercooling cycle layout.

there are two compressors: the main compressor (MC), that provides the most pressurized stream to the low-temperature recuperator (LTR); and the auxiliary compressor (AC), that connects to the high-temperature recuperator (HTR). The new PCHE proposed in this paper performs as the source heat exchanger (SHX), located upstream the turbine (T), on the line of highest pressure and temperature of the supercritical cycle. The isentropic efficiencies of both the turbine and the compressors have been set at 92% and 88%, respectively (Linares et al., 2020).

The two recuperators (LTR and HTR) are modeled as conventional PCHEs, for sCO_2-to-sCO_2 heat transfer. So, the thermal model implemented for these HXs is very similar to that exposed in Section 2.1, but

with the recommended geometrical parameters of PCHE [6]: semi-circular microchannels of 2 mm diameter for both streams. The maximum pressure drop of the sCO_2 in the recuperators has been set at 0.4 bar (Medrano et al., 2007), whereas the maximum pressure drop of the SHX (dP_{sCO2}) is a variable to optimize (Section 4). In the same way, the temperature approach ($TA_{MS-sCO2}$) for the balanced SHX is also a variable to optimize (Section 4). No shape pressure drops have been considered in the inlet/outlet of the heat exchangers, neither in the pipes inside the cycle. As the operation temperature of these heat exchangers is lower than the SHX, a discretization calculation process has been carried out to take into account the variation of the properties of the sCO_2.

The dry cooling is also assumed in the three cycles, so the pre-cooler (PC) and the intercooler (IC) (the latter one is only presented in the partial-cooling and intercooling layouts), are air-cooled heat exchangers. These HXs are modeled as compact heat exchangers (CHXs) with finned circular tubes, core sCF-734 (Hruska et al., 2016). The power consumption has been set to 50 kW per heat exchanger, adopting an electro-mechanical efficiency of 75% in the fans of these HXs (Linares et al., 2020).

Although dP_{sCO2} and $TA_{MS-sCO2}$ in the SHX are the variables of the parametric analysis for the thermoeconomic optimization (Section 4), these values have been set at 0.5 bar and 10 °C, respectively, in order to simulate a base-line case of each of the three supercritical cycles. Table 6 shows the thermodynamic properties of the state points following the numbering marked in Fig. 7a (recompression), Fig. 7b (intercooling) and Fig. 7c (partial-cooling).

In Table 6, the cycle power is the power supplied by the turbine minus the power consumed by all the compressors (Eq. (1)), and the

Table 6
Thermodynamic properties of the state points of supercritical cycles.

	Recompression cycle			Intercooling cycle			Partial-cooling cycle		
	P (bar)	T (°C)	h (kJ/kg)	P (bar)	T (°C)	h (kJ/kg)	P (bar)	T (°C)	h (kJ/kg)
1	200	688	701.3	250	688	699.5	250	688	699.5
2	86.2	574.1	566.5	86.2	545.1	531.4	86.2	545.1	531.4
3	85.8	224.2	158.4	85.8	212.3	144.9	85.8	142.3	62.99
4	85.4	122.9	39.09	85.4	97.71	5.775	85.4	85.38	−12.13
5	85	50	−80.9	85	50	−80.9	85	50	−80.9
6	201.2	118.3	−41.57	108.5	68.92	−71.05	120.3	77.05	−66.64
7	200.8	219.6	117.4	108.1	50	−147.6	119.9	50	−170.2
8	200.8	212	107.2	251.2	92.71	−118.9	251.2	80.18	−147.1
9	200.8	217.7	114.9	250.8	207.3	86.56	250.8	137.1	−26.99
10	200.4	545.6	522.9	250.8	205.8	84.32	250.8	136.3	−28.48
11				250.8	206.8	85.84	250.8	136.8	−27.54
12				250.4	508	472.4	250.4	482.8	440.9
Cycle power (MW)	50.00			50.00					
							50.00		
Source thermal power (MW$_{th}$)	100.99			97.40					
							103.42		
Cycle efficiency (%)	49.57			51.40					
							48.41		

cycle efficiency is the ratio between the cycle power and the thermal power transferred to the sCO$_2$ from the hot MS (Eq. (2)), by means of the PCHE proposed in this work.

$$\dot{W}_{cycle} = \dot{W}_T - \dot{W}_{MC1} - \dot{W}_{MC2} - \dot{W}_{AC} \qquad (1)$$

$$\eta_{cycle} = \frac{\dot{W}_{cycle}}{\dot{Q}_{th,source}} \qquad (2)$$

The layout with higher cycle efficiency is the intercooling cycle, as stated in the introduction. The thermal power required is therefore less than in the other layouts, for the same power cycle, which yields to a reduction in the required MS inventory. On the other hand, the partial cooling cycle exhibits the larger temperature difference of the sCO$_2$ through the SHX (temperature at points 12 and 1 in Table 6), which also causes a reduction in the MS volume. So, a global analysis of the total STPP performance is required in order to assess the best configuration. This analysis is described in Section 4, when analyzing the optimum sizing of the SHX.

3.2. The solar field

The central receiver of the solar field has been designed as a tubular cavity-type. This configuration has been preferred over the external-type for working at high temperature (>700 °C), as the cavity receiver exhibits lower radiation heat loss and higher convective heat loss than external receivers (Falcone, 1986). This characteristic makes cavity receivers more suitable when the working temperature increases and the radiation heat loss becomes critical.

Basic thermal or geometrical parameters of this receiver have been chosen or calculated according to technical literature. The allowable peak flux density has been set to 1 MW/m^2, while the average flux density has been set to 0.4 MW/m^2, both values recommended for cavity molten salt receivers (Liao et al., 2014); these values are less than those recommended for external receivers, because the inner surfaces of the receiver are exposed to re-radiation, which may lead to overheating; and this is also the reason because the cavity receivers are larger than the external receivers, for the same incident power. The aspect ratio (height-to-diameter ratio) should be in the range of 0.7–1 (Stalin, 2016) for these cavity receivers, so a value of 0.7 is selected. The lip height (aperture-to-panel height ratio) is set to 0.7, also according to literature (Zavoico, 2001); this value is a trade-off between the convective heat loss decrease and the radiation spillage increase if the aperture becomes very small.

The receiver tube diameter can vary between 20 mm and 45 mm, and the wall thickness is limited to commercial values. The value of the diameter should be optimized in order to improve the heat transfer to the molten salt, by increasing its velocity and the Reynolds number, with a limited increase in the pressure drop. For this analysis, it has been fixed the average molten salt velocity to 2 m/s through all the receivers
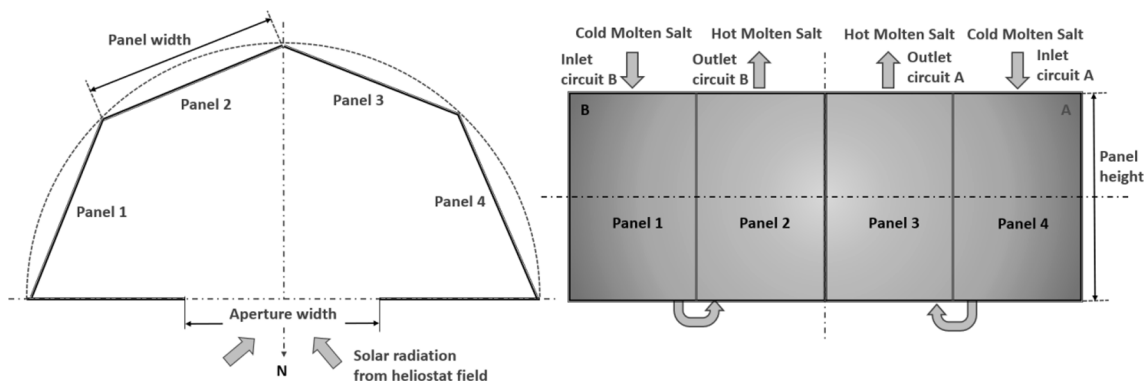

Fig. 8. Fluid flow layout and configuration of the cavity receiver.

Table 7
Main characteristics of the cavity receivers for each layout.

Receiver	Recompression	Intercooling	Partial-cooling
Sizing and geometrical characteristics			
Number of panels	4	4	4
Pannel width (m)	7.32	7.13	7.26
Pannel height (m)	13.40	13.04	13.28
Aperture width (m)	19.14	18.63	18.97
Aperture height (m)	10.05	9.78	9.96
Number of passes	2	2	2
Outer/inner diameter (mm)	38.1/33.88 (1-1/2″ BWG 14)	31.75/28.45 (1-1/4″ BWG 16)	25.4/22.91 (1″ BWG 18)
Thermal characteristics			
Thermal power (MWth)	201.984	194.804	206.838
Solar multiple	2	2	2
Cycle thermal power (MWth)	100.992	97.402	103.419
Inlet MS temperature	544.9	522.8	498.4
Outlet MS temperature	700	700	700
Incident heat (MWth)	253.65	241.19	251.33
Thermal efficiency	79.63	80.77	82.30
Themal loss from each panel			
Convection heat loss (kWth)			
Panels 1&4 (Side panels)	832.26	796.99	830.02
Panels 2&3 (Central panels)	734.34	718.32	776.18
Solar radiation heat loss (kWth)			
Panels 1&4 (Side panels)	415.40	395.00	2334.26
Panels 2&3 (Central panels)	454.98	432.64	2733.18
Infrared radiation heat loss (kWth)			
Panels 1&4 (Side panels)	1419.56	1221.11	6249.70
Panels 2&3 (Central panels)	1830.86	1631.60	9322.70

Table 8
Optical and thermal performance of the heliostat field for each STPP considered (Simulated by SolarPILOT [40]).

	Recompression	Intercooling	Partial-cooling
Total plant cost (Mio.$)	173.39	168.15	173.16
Simulated heliostat area (m^2)	669,755	655,028	669,755
Simulated heliostat count	4639	4537	4639
Tower optical height (m)	180	172	180
Solar field optical efficiency (%)	83.52	83.43	84.74

2010; Boudaoud et al., 2015). On one hand, it accounts for the solar and infrared radiosity exchange inside the cavity, applying the semi-gray approximation to an enclosure, as the aperture is considered a "virtual" surface (Siegel and Howell, 2002). On the other hand, it calculates the convection heat loss from each of the receiver panels, by means of the Clausing equation, which gives more accurate results than other more simplified equations (Samanes et al., 2015). Table 7 summarizes the main thermal and geometrical parameters of the cavity receivers for the three supercritical layouts (recompression, partial-cooling and intercooling).

As seen in Table 7, the thermal efficiency of the receiver increases as the MS temperature in the receiver decreases, so the receiver for the partial-cooling configuration is the one that exhibits a larger thermal efficiency. The thermal efficiency of the receiver is calculated by equation (3):

$$\eta_{th} = \frac{\dot{Q}_{useful}}{\dot{Q}_{incident}} = \frac{\dot{Q}_{useful}}{\dot{Q}_{useful} + \dot{Q}_{loss,total}} \tag{3}$$

The heat losses from the receiver are described by Eqs. (4)–(7). The total radiation heat loss is the sum of the solar and infrared radiosity leaving each surface (Eq. (5)). Both radiosities have been calculated applied the semi-gray theory. As said above, convection heat loss is calculated by Clausing correlation, Eq. (7).

$$\dot{Q}_{loss,total}(W) = \dot{Q}_{loss,rad}(W) + \dot{Q}_{loss,conv}(W) \tag{4}$$

$$\dot{Q}_{loss,rad}(W) = \sum_i A_i \cdot J_i^s + A_i \cdot J_i^r \tag{5}$$

$$\dot{Q}_{loss,conv}(W) = \sum_i A_i \cdot \dot{q}_{conv,i} = \sum_i A_i \cdot h_{conv,i} \cdot (T_i - T_{amb}) \tag{6}$$

$$Nu_i = \frac{h_{conv,i} \cdot L_{c,i}}{k_f} = 0.082 \cdot Ra^{1/3} \cdot \left[-0.9 + 2.4 \cdot \frac{T_{w,i}}{T_{amb}} - 0.5 \cdot \left(\frac{T_{w,i}}{T_{amb}} \right)^2 \right] \cdot z(Z_{w,i}) \tag{7}$$

In the above equations, $\dot{Q}_{loss,total}$ (W) is the total heat loss from the receiver; $\dot{Q}_{loss,rad}$(W) is the radiation heat loss, and $\dot{Q}_{loss,conv}$ (W) is the convection heat loss; sub-indexes i/j refers to the surface of the cavity, and super-indexes s/r stands for the solar/infrared radiosity; J (W/m^2) is the radiosity from each surface; A (m^2) is area of each surface; h_{conv} (W/m^2/°C) is the convection heat transfer coefficient, calculated by equation (5); Ra is the Rayleigh number, $T_{w,i}$ (K) is the temperature of the surface i of the cavity, T_{amb} (K) is the ambient temperature and $z(Z_{w,i})$ is the surface orientation, where $Z_{w,i}$ is the angle between the z-axis and the normal vector to the surface.

For each receiver configuration, it is necessary to calculate the optical performance of the associated heliostat field. The heliostat field has been oversized with a solar multiple of 2, as a compromise between the plant dispatchability and the receiver dimensions, which are larger for

simulated, while the tube diameter is changed from one case to another, in order to keep the velocity to a constant value.

The material for the tubes is Hastelloy N, whose main properties are shown in Table 3. In this case, the material choice is justified because the irradiation resistance is good, as well as the salt corrosion resistance. The maximum allowable stress of Hastelloy N is lower than that of Haynes 242, but this is not important as the receiver is not pressurized. There is not any commercial selective coating for tubes that withstand high temperature and does not degrade in air; for that reason, the tubes are coated by pyromark paint with a solar absorptivity equal to 0.96 and a thermal emissivity of 0.88.

Regarding the fluid flow path selection, there are several patterns described in (Feierabend, 2010). The one adopted in this work is described in (Montes et al., 2012); it consists of dividing the total flow into two streams, and each of them circulates through serially connected, adjacent panels. The fluid enters the receiver through the outer panels and exit from the inner panels. In this way, the fluid pattern is adapted to the symmetry of the solar image, and the molten salt is circulated from the zone of lower solar flux to the zone of higher solar flux. The receiver configuration and the fluid layout can be seen in Fig. 8.

The thermal model developed for the receiver introduces two main improvements, compared to other models in the literature (Li et al.,

cavity-type compared to external designs for the same power. The solar field has been simulated with SolarPILOT, a program developed by NREL (2020) and described in (Wagner and Wendelin, 2018). Solar-PILOT incorporates data from SAM software (Freeman et al., 2018), so it also provides an economic assessment of the solar field investment, including the tower and receiver. Table 8 summarizes the main characteristics of the simulated solar fields for each of the three STPPs considered.

At last, a brief description is given about the molten salt thermal storage. This system consists of two tanks of molten salts, which have been sized to provide the nominal thermal power to the supercritical cycle for 6 h, with a charging time of 6 h, i.e., a solar multiple of 2. For the simulation in nominal conditions, it is considered a pressure drop of 5 bar in the storage and the solar receiver systems. As seen in Fig. 6, the storage system is provided by two pumps. The high temperature pump (HTP) circulated the molten salt flow from the hot tank whereas the low temperature pump (LTP) drives this fluid from the cold pump. As a solar multiple of 2 has been assumed, the mass flow rate in the LTP is 2 times the one in the HTP. Both pumps are supposed with an electromechanical efficiency of 75%. The net electricity power supplied by the STPP (Eq. (8)) accounts for the consumption of both the molten salt pumps and the fans of the dry cooling, described in Section 3.1, also with an electromechanical efficiency of 75%. In Eq. (8), η_g is the generator efficiency, taken as 97% (Linares et al., 2017). Finally, the net efficiency is defined as the ratio of the net electricity power to the thermal power in the SHX, Eq. (9).

$$\dot{W}_{net} = \eta_g \cdot \dot{W}_{cycle} - \dot{W}_{HTP} - \dot{W}_{LTP} - \dot{W}_{CP} \quad (8)$$

$$\eta_{net,cycle} = \frac{\dot{W}_{net}}{\dot{Q}_{th,source}} \quad (9)$$

To summarize this section, the thermal model of the STPP has been properly described ann implemented. This is the framework in which the optimization of the proposed PCHE is accomplished, because it is necessary to consider how the design of this PCHE impacts the STPP global performance.

4. Thermo-economic analysis and optimization

The optimum size and cost of the proposed PCHE is calculated by means of savings-to-investment ratio (SIR) method (Shouman, 2018), referred to the annual cost. In this way, the optimum heat exchanger is the one that maximizes the figure of merit showed in Eq. (10).

$$SIR_{PCHE} = \frac{C_{savingsPCHE}}{CRF \cdot C_{0,PCHE}} \quad (10)$$

In this equation, SIR_{PCHE} is the savings-to-investment ratio, which is the ratio of annual savings to the annualized investment in the base PCHE. It is important to appoint that the general criterion of the SIR method to consider a project as profitable is that SIR > 1. In this particular case, as the discussion is about a different design of a heat exchanger already in the power plant, the new design of PCHE will be profitable if SIR > 0.

The savings costs $C_{savings}$ account for the investment savings in a more limited PCHE and the lack of benefit by producing less electricity, since the STPP global operation is worse as the PCHE performance is worse.

$$C_{savingsPCHE} = CRF \cdot \left(C_{0,PCHE} - C_{PCHE}\right) - CELF \cdot C_E \cdot Y \cdot Q_{th,source} \cdot \left(\eta_{0net,cycle} - \eta_{net,cycle}\right) \quad (11)$$

In the above equation, CRF is the capital-recovery factor and CELF is the constant-escalation levelization factor, both defined below; C_E is the electricity cost, 61.2 $/MWh, which is based on the average market price at USA (EIA, 2018); Y is the yearly operation time, calculated for a

Table 9
Parameters for the thermo-economic analysis and optimization.

Economic parameters	
Effective discount rate i_{eff} (%)	7
Capital recovery factor CRF (%)	8.58
Nominal escalation rate (%)	5
k (%)	98.13
Constant escalation levelization factor (CELF)	19.74

solar multiple equal to 2: $Y = 365 * 12$ h; Q_{th} (W) is the thermal power supplied by the PCHE; finally, C_{PCHE} is the investment cost in the PCHE, and $\eta_{net,cycle}$ is the net efficiency of the supercritical cycle, defined as Eq. (9); if these last two parameters are affected by the sub-index 0 is because they are referred to the base case: a PCHE with $TA_{MS-sCO2} = 10$ °C and $dP_{sCO2} = 0.5$ bar.

The investment cost C_{PCHE} can be estimated from the mass of the heat exchanger and the cost factor of material ($CM_{PCHE} = 120$ $/kg for Haynes 242), Eq. (12). This estimation has been widely used by many authors to calculate the cost of PCHEs (Dostal, 2004; Kim et al., 2008; Yoon et al., 2014).

$$C_{PCHE} = M_{PCHE} \cdot CM_{PCHE} \quad (12)$$

The mass of the PCHE is easily calculated by means of the metal density (9050 kg/m³ for Haynes 242) and the fraction of metal per m³ of the heat exchanger, also called the core volume. In the case of this PCHE, the core volume is calculated by the ratio of free area to frontal area, defined by Eq. (A.4) in the Appendix A.

$$M_{PCHE} = \rho_{PCHE} \cdot V_{core,PCHE} = \rho_{PCHE} \cdot V_{PCHE} \cdot (1 - \sigma) \quad (13)$$

The capital-recovery factor (CRF) and the constant-escalation levelization factor (CELF) are calculated by means of Eq. (14) and (15).

$$CRF = \frac{i_{eff} \cdot \left(1 + i_{eff}\right)^n}{\left(1 + i_{eff}\right)^n - 1} \quad (14)$$

$$CELF = CRF \cdot \frac{k \cdot \left(1 - k^n\right)}{(1 - k)} \quad (15)$$

where

$$k = \frac{1 + r_n}{1 + i_{eff}}$$

In the above equations, i_{eff} (%) is the effective discount rate, and n (years) is the economic life o span period of the power plant; r_n is the nominal escalation rate, which represents the annual change in cost and includes the effects of both the real escalation rate r_r and the inflation r_i. The values of the parameters defined above are summarized in Table 9.

For the optimization, the SIR method is applied to different configurations of the proposed PCHE, based on the different temperature approach between the two streams (from 10 °C to 50 °C) and the different pressure drop in the sCO_2 (from 0.5 bar to 2 bar). The PCHE investment cost decreases by increasing both dP_{sCO2} and $TA_{MS-sCO2}$, but the electricity revenues also decrease, as pumping power increases and the HX performance is worse, affecting the global performance of the plant. This different trend in costs yields to an optimal PCHE configuration that minimizes those costs. These results are showed in Fig. 9 (recompression), Fig. 10 (intercooling) and Fig. 11 (partial-cooling).

It can be seen in the above figures that there is a configuration that maximizes the saving-to-investment ratios, regarding to the base PCHE, as summarized Table 10. The inversion cost of the PCHE follows the same pattern.

Table 10 summarizes the thermal parameters values (dP_{sCO2} and $TA_{MS-sCO2}$) and the investment cost C_{PCHE} for both the base and the optimized case. According to this table, the optimum temperature approach is greater for the configuration with a larger temperature
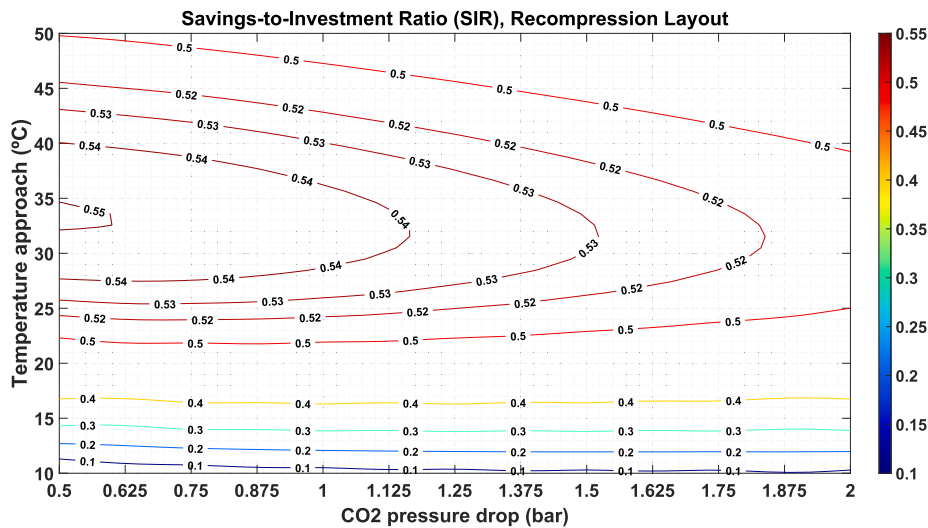
Fig. 9. Savings-to -investment ratio for the source heat exchanger (PCHE) in the recompression layout.
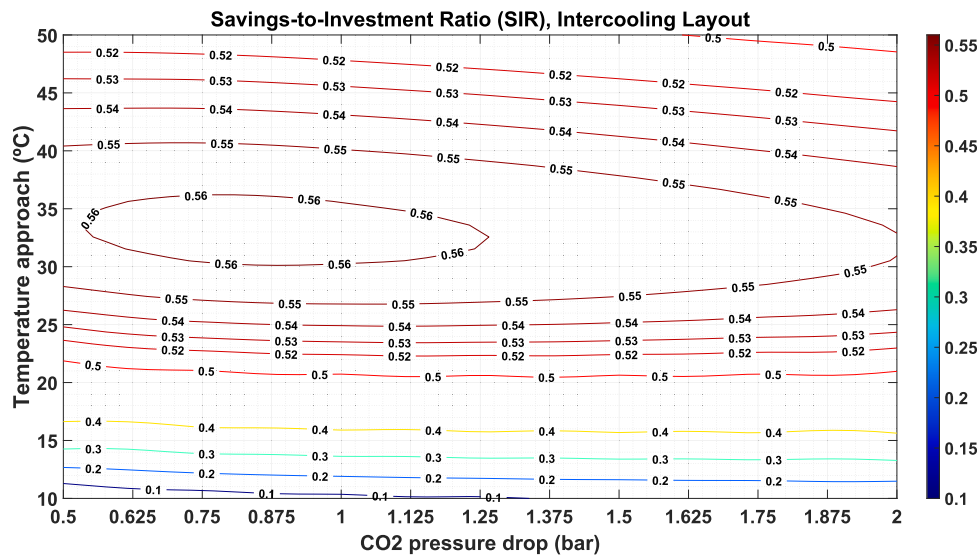

Fig. 10. Savings-to -investment ratio for the source heat exchanger (PCHE) in the intercooling layout.

difference in the PCHE (partial-cooling), whereas the greater pressure drop occurs in the configurations with higher pressure at the inlet of this PCHE (partial-cooling and intercooling).

To finish this section, the fixed capital investment (FCI, Mio.$) and the levelized cost of electricity (LCOE) has been calculated, for the base case (SHX with TA = 5 °C and dP_{sCO2} = 0.5 bar) and the optimized case of each of the three supercritical layouts simulated. Each investment item includes purchase equipment cost (PEC), the share in pipes, instrumentation and control (118% of PEC) and indirect cost (25% of PEC), according to (Fleming et al., 2013). The LCOE has been estimated based on the capital cost and the annual production of the net power and the total operation time.

Firstly, Table 11 shows that the investment in the SHX (PCHE) is greatly reduced by this optimization process, to 25% of its base value. Secondly, it is also observed that for the base configurations, the intercooling is the one with lowest costs LCOE. Nevertheless, for the optimized layouts, partial-cooling exhibits the lowest FCI, followed by intercoling and finally recompression; the same trend is observed in the case of the LCOE. This is due to the greater investment reduction of the SHX since, having a higher temperature difference, the temperature approach can be increased slightly (40 °C compared to 35 °C in the other

layouts), without an important impact on the net efficiency.

5. Conclusions

A new MS-to-sCO$_2$ heat exchanger design between the solar field and the power cycle in supercritical STPPs is proposed in this work. This design is based on the printed circuit heat exchanger (PCHE), with a conventional semi-circular channel for sCO$_2$ and a circular channel of greater hydraulic diameter, for the molten salt. This design is intended to withstand the pressure difference between the two phases and prevent molten salt plugging, without a performance decrease. The thermal model of the PCHE is presented and validated by CFD. Although a mechanical calculation has been made to ensure a minimum thickness between channels, a future work will be a specific thermo-mechanical stress analysis of the proposed PCHE. This design is a new possibility to the technical feasibility of STPPs coupled to supercritical cycles, since there are few studies about the design of this type of MS-to-sCO$_2$ HXs.

A thermo-economic optimization of this PCHE is also accomplished by the savings-to-investment method. For this optimization, it is considered not only the PCHE, but also the complete STPP in which this source heat exchanger (SHX) is located. With this aim, three
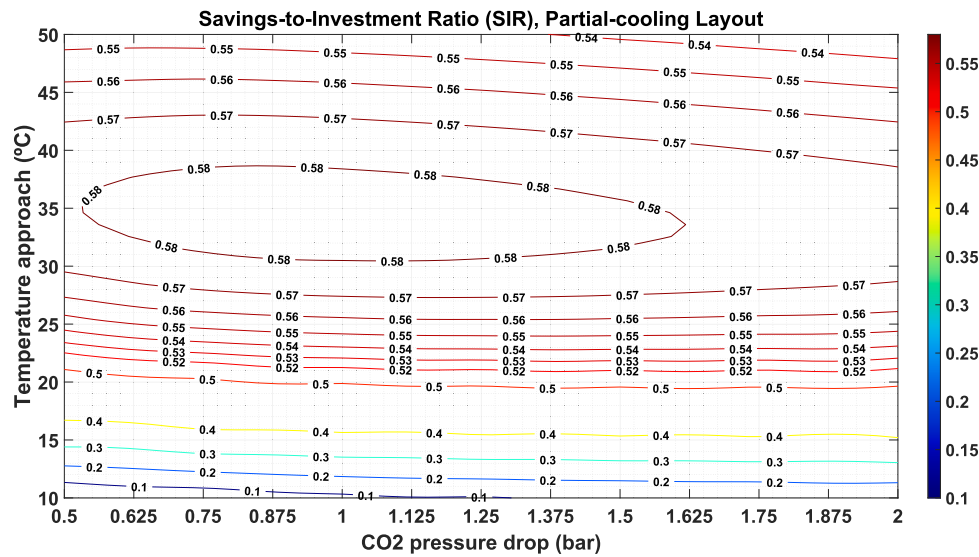
Fig. 11. Savings-to-investment ratio for the source heat exchanger (PCHE) in the partial-cooling layout.

Table 10
Thermal parameters and purchase equipment cost for both the base and optimized PCHE configuration.

Supercritical layout	Base PCHE configuration			Optimized PCHE configuration		
	$TA_{MS\text{-}sCO_2}$ (°C)	dP_{sCO_2} (bar)	C_{PCHE} (Mio.$)	$TA_{MS\text{-}sCO_2}$ (°C)	dP_{sCO_2} (bar)	C_{PCHE} (Mio.$)
Recompression	10	0.5	38.769	35	0.5	9.427
Intercooling	10	0.5	37.417	35	1	8.565
Partial cooling	10	0.5	40.456	40	1	7.924

supercritical layouts have been selected: recompression, intercooling and partial-cooling. The thermo-economic optimization yields to the following conclusions:

– If the temperature approach and the pressure drop in the PCHE are increased, there is a decrease in the heat exchange area, which lowers the investment cost but reduces the revenues, not only by increasing the pumping power, but also by the worse PCHE performance, which affects the plant net efficiency.
– The different trend in costs yields to an optimal size and performance of the PCHE proposed, which maximizes the savings-to-investment ratio and minimizes the FCI and the LCOE, for each of the supercritical configurations analysed.
– For the base case, the PCHE with a greatest investment cost is the one of the partial-cooling, followed by the recompression and finally the intercooling ($PHCE_{0,pc} > PHCE_{0,r} > PHCE_{0,ic}$); this variation is

basically due to the thermal power required in the SHX by each of the cycles.
– In the optimized case, this trend in inverted: the optimized PCHE with the lowest investment cost is the one locates in the partial-cooling layout, followed by the intercooling and finally the recompression ($PHCE_{pc} < PHCE_{ic} < PHCE_r$). The cost reduction is greater in the partial-cooling due to the larger temperature difference of the sCO_2 (and the molten salt) in the SHX, allowing a higher temperature approach without greatly affecting performance.
– If the complete supercritical STPP is analysed, the best optimized layout is the partial-cooling (LCOE = 135.7 $/MWh$_e$), followed by intercooling (LCOE = 140.1 $/MWh$_e$) and recompression (LCOE = 160 $/MWh$_e$).

These results, although accounting for the whole solar plant, refer only to the optimization of the PCHE between the molten salt from the solar field and the supercritical cycle. A global optimization process of all plant components would be necessary in the future. It can be concluded, however, that partial-cooling and intercooling configurations yield to lower FCI and LCOE than conventional recompression layout. This is a very interesting result, as intercooling cycle has not been considered for the moment as a possible candidate to couple to STPP.

Declaration of Competing Interest

The authors declare that they have no known competing financial interests or personal relationships that could have appeared to influence the work reported in this paper.

Table 11
Summary of the fixed capital investments and LCOE for the base-line and optimized layouts, for each configuration (RC = recompression cycle; IC = intercooling cycle; PC = partial cooling cycle).

	Base RC	Optimized RC	Base IC	Optimized IC	Base PC	Optimized PC
SHX (PCHE) (Mio.$)	**105.6**	**25.7**	**102.0**	**23.3**	**110.2**	**21.6**
Recuperators (LTR + HTR) (Mio.$)	56.4	55.5	33.9	33.3	20.7	20.6
Precooler CO2/AIR (Mio.$)	6.8	6.8	11.2	11.3	11.8	11.8
TM (Mio.$)	49.2	48.5	43.0	42.5	43.0	42.6
TES (Mio.$)	75.0	75.0	59.9	60.2	56.6	56.6
Solar Field (Mio.$)	173.4	173.4	168.2	168.2	173.2	173.2
FCI (Mio.$)	**466.5**	**385.0**	**418.1**	**338.8**	**415.5**	**326.4**
LCOE [$/MWhe]	**190.5**	**160.0**	**170.3**	**140.1**	**172.7**	**135.7**

Appendix A

This appendix summarizes the basic equations describing the thermal model of the PCHE. Once the inlet/outlet properties are defined, the total mass flow rate of each fluid is determined, and can be calculated through the basic energy balance, Eq. (A.1):

$$\dot{Q}_{PCHE} = \dot{m}_1 \cdot (h_{1,in} - h_{1,out}) = \dot{m}_2 \cdot (h_{2,out} - h_{2,in}) \tag{A.1}$$

In the above equation, sub-index 1 refers to the primary fluid, that is, the molten salt through the circular channel, whereas the sub-index 2 refers to the secondary fluid, that is, the sCO$_2$ through the semi-circular channels; $\dot{Q}$ (W) is the thermal power of the PCHE; $\dot{m}$ (kg/s) is the mass flow rate; and h (J/kg) is the specific enthalpy.

For both fluids, the cross-flow area is calculated based on the averaged density and the maximum velocity, Eq. (A.2).

$$A_{c,i} = \frac{\dot{m}_i}{\rho_{ave,i} \cdot u_{max,i}} \tag{A.2}$$

In Eq. (A.2), the subindex i = 1 (MS), 2 (sCO$_2$); A_c(m^2) is the cross flow area; ρ_{ave}(kg/m^3) is the average density; and u_{max}(m/s)is the maximum velocity of the stream. As $A_{c,1} = A_{c,2}$, the maximum velocities are related because the average properties and the mass flow rates have been previously set.

The frontal area of the PCHE is calculated from the cross-flow area by Eq. (A.3):

$$A_f = \frac{A_{c,1} + A_{c,2}}{\sigma} \tag{A.3}$$

In Eq. (A.3), σ is the ratio of free flow area to frontal area, and it can be calculated based on the geometric parameters defined in one thermal unit.

$$\sigma = \frac{\pi \cdot (d_1^2 + d_2^2)/4}{(2 \cdot t_{p1} + 2 \cdot t_{p2}) \cdot p_c} \tag{A.4}$$

Once the cross-section parameters are defined, and the mass flow rate per channel, it is possible to model the heat transfer from the MS to the sCO$_2$ by means of a two-dimensional thermo-hydraulic process. This process consists of dividing the PCHE in N heat exchanger elements (HXE) of the same thermal duty:$\dot{Q}_{HXE} = \dot{Q}/N$. These HXEs are short enough to be able to approximate to average temperatures and properties, both for the MS and the sCO$_2$, with great accuracy. This is clear for the MS, which is an incompressible fluid approximately, but also for the sCO$_2$, as this fluid is at very high temperature and far away from the critical point.

The basic equation of heat transfer, Eq. (A.5), is applied to each of these HXE, in order to calculate its length.

$$\dot{Q}_{HXE} = U_{HXE} \cdot A_{HXE} \cdot \Delta T_m \rightarrow L_{HXE} = \frac{\dot{Q}_{HXE}}{U_{HXE} \cdot N_{ch} \cdot P_{HXE} \cdot \Delta T_m} \tag{A.5}$$

A_{HXE}(m^2) is the heat transfer area of each elementary HXE; ΔT_m(°C) is the mean temperature, equal to the constant temperature difference between both streams, as the PCHE is balanced counter-flow heat exchanger; L_{HXE}(m) is the length of each elementary HX;N_{ch} is the number of channels of the MS/sCO$_2$ in each elementary HX; P_{HXE}(m) is the perimeter of the semi-circular/circular channel in each HXE; and, finally, U_{HXE}(W/m^2/°C) is the overall heat transfer coefficient of the counterflow elementary PCHE, given by Eq. (A.6).

$$U_{HXE} = \frac{1}{\frac{1}{h_{conv1}} + \frac{1}{U_w} + \frac{1}{h_{conv2}}} \tag{A.6}$$

U_W (W/m^2 °C) is the thermal transfer coefficient for the wall between channels, that accounts for an equivalent thickness of the semi-circular cross section of these channels (Ariu, 2014); h_{conv} (W/m^2/°C) is the convection heat transfer coefficient.

For the small ducts of compact heat exchangers, Hesselgreaves (2017) recommends using the Gnielinski correlation for fully-developed turbulent flow ($Re > 2300$) in straight semi-circular channels, Eq. (A.7).

$$Nu_{Dh} = \frac{(f_c/8) \cdot (Re_{Dh} - 1000) \cdot Pr}{1 + 12.7 \cdot \left(\sqrt{\frac{f_c}{8}}\right) \cdot (Pr^{2/3} - 1)} \cdot \left(\frac{Pr}{Pr_{si}}\right)^{0.11} \tag{A.7}$$

$$where:$$
$$f_c = [1.82 \cdot log(Re_{Dh}) - 1.64]^{-2}$$

This correlation is valid for Reynolds numbers ranging from 2300 to 5x10^5 and Prandtl numbers from 0.5 to 2000. In the above equation f_c is the friction factor, calculated as needed from the Filonenko correlation (Gnielinski); Re_{Dh} is the *Reynolds* number based on the inner hydraulic diameter; Pr is *Prandtl* number at the bulk fluid temperature; Pr_{si} is the *Prandtl* number at the inner duct temperature, t_{si}.

Gnielinski correlation is applicable for the sCO$_2$ but, for the MS in the circular duct, the flow is fully-developed laminar and then, the following correlation is recommended (Hesselgreaves, 2017):

$$Nu = 4.3636 \; for \; Re_{Dh} < 2300, \; circular \; ducts \tag{A.8}$$

The value of the Nusselt number calculated by Gnielinski correlation (Eq. (A.7)) at $Re = 2300$ is not 4.3636 (Eq. (A.8)), so it would be a discontinuity at this point. To eliminate such discontinuity, it has been considered a transitional region between 2300 and 5000, in which the Nusselt

number is calculated by linear interpolation (Eq. (A.9)), in the same way as described in (Dostal, 2004).

$$Nu = 4.3636 + \frac{(Nu_{5000} - 4.3636) \cdot (Re_{Dh} - 2300)}{5000 - 2300} \ for \ 2300 < Re_{Dh} < 5000 \tag{A.9}$$

Once the length of the heat exchanger is obtained, the friction pressure loss ΔP can be calculated, by means of the *Darcy–Weisbach* equation evaluated at the averaged values of each stream in the elementary PCHE (Eq. (A.10)).

$$\Delta P_{HXE} = \frac{1}{2} \cdot f_D \cdot \left(\frac{L_{HXE}}{D_h}\right) \cdot \rho_{ave} \cdot u_{ave}^2 \tag{A.10}$$

where D_h (m) is the hydraulic diameter of the duct; ρ (kg/m^3) is the average fluid density; u (m/s) is the average fluid velocity; and f_D is the Darcy friction factor, that is four times the *Fanning* friction factor, f_F: $f_D = 4 \cdot f_F$. This friction factor can be calculated by the following two correlations, developed for smooth ducts (Hesselgreaves, 2017): Hagen-Poiseulle for laminar flow ($Re_{Dh} \le 2300$), and Techo et al. for turbulent flow ($10^4 \le Re_{Dh} \le 10^7$).

$$\begin{cases} f_F = \frac{16}{Re_{Dh}} \ for \ Re_{Dh} \le 2300 \\ \frac{1}{f_F} = 1.7372 \cdot \ln\left[\frac{Re_{Dh}}{1.964 \cdot \ln(Re_{Dh}) - 3.8215}\right] \ for \ 10^4 \le Re_{Dh} \le 10^7 \end{cases} \tag{A.11}$$

For the transition region, $2300 < Re_{Dh} < 10^4$, the friction factor is calculated by a linear approximation weighted with the *Reynolds* number, similar to that already applied to the Nusselt number for transitional flow.

A more detailed estimation of the friction factor for the transition regime is explained in (Dostal, 2004). That characterization is not necessary for the PCHE presented in this paper, as the working conditions of the sCO$_2$ and the chloride MS are well stablished in the turbulent and laminar regimes, respectively. It should be noted that both the Nusselt number and the friction factor correlations have been developed for smooth ducts. Rough ducts are unlikely to be found in a PCHE, since the surfaces are usually formed from well-rolled sheet.

The total pressure drop in the PCHE accounts for the friction loss in the straight ducts, calculated by Eq. (A.10), and the shape pressure losses at the inlet and outlet of the heat exchanger. Both can be evaluated by Eq. (A.12).

$$\Delta P_{in/out} = \frac{1}{2} \cdot C \cdot \rho_{ave} \cdot u_{ave}^2 \tag{A.12}$$

where C is the shape loss coefficient that is taken to be 0.5 at the inlet and 1.0 at the outlet from the PCHE (Dostal, 2004).

References

ANSYS, Inc. ANSYS CFX-Solver Theory Guide. ANSYS Copyright 2009. https://www.ansys.com/.

Ariu, V., 2014. Heat exchanger analysis for innovative molten salt fast reactor. Master Thesis. ETH Zürich – EPF Lausanne.

ASME Boiler and Pressure Vessel Committee, American Society of Mechanical Engineers, ASME Boiler and Pressure Vessel Committee, Subcommittee on Pressure Vessels, 2010. Rules for construction of pressure vessels. An international code VIII, Division 1 VIII, Division 1. American Society of Mechanical Engineers, New York, N.Y.

Boudaoud, S., Khellaf, A., Mohammedi, K., Behar, O., 2015. Thermal performance prediction and sensitivity analysis for future deployment of molten salt cavity receiver solar power plants in Algeria. Energy Convers. Manage. 89, 655–664. https://doi.org/10.1016/j.enconman.2014.10.033.

Crespi, F., Gavagnin, G., Sánchez, D., Martínez, G.S., 2017. Supercritical carbon dioxide cycles for power generation: A review. Appl. Energy 195, 152–183. https://doi.org/10.1016/j.apenergy.2017.02.048.

Dewson, S.J., Li, X., 2005. Selection criteria for the high temperature reactor intermediate heat exchanger. In: Proceedings of the American Nuclear Society - International Congress on Advances in Nuclear Power Plants 2005, ICAPP'05. 3. 1712–1719.

Dostal, V., 2004. A supercritical carbon dioxide cycle for next generation nuclear reactors. Thesis (Sc. D.). Massachusetts Institute of Technology, Dept. of Nuclear Engineering.

EIA - Energy Information Administration, 2018. Electric Power Annual 2018. Average retail price of electricity to ultimate consumers by end-use sector. www.eia.doe.gov.

Falcone, P.K., 1986. A handbook for solar central receiver design (No. SAND-86-8009, 6545992). 10.2172/6545992.

Feierabend, L., 2010. Thermal Model Development and Simulation of Cavity-type Solar Central Receiver Systems. University of Wisconsin–Madison.

Fleming, D.D., Holschuh, Thomas Vernon, Conboy, T.M., Pasch, J.J., Wright, S.A., Rochau, G.E., Fuller, R.L., 2013. Scaling considerations for a multi-megawatt class supercritical CO2 brayton cycle and commercialization. (No. SAND2013-9106, 1111079). 10.2172/1111079.

Freeman, J.M., DiOrio, N.A., Blair, N.J., Neises, T.W., Wagner, M.J., Gilman, P., Janzou, S., 2018. System Advisor Model (SAM) General Description (Version 2017.9.5) (No. NREL/TP–6A20-70414, 1440404). 10.2172/1440404.

Fu, Q., Ding, J., Lao, J., Wang, W., Lu, J., 2019. Thermal-hydraulic performance of printed circuit heat exchanger with supercritical carbon dioxide airfoil fin passage and molten salt straight passage. Appl. Energy 247, 594–604. https://doi.org/10.1016/j.apenergy.2019.04.049.

Heatric. https://www.heatric.com/.

Hesselgreaves, J.E., 2017. Compact heat exchangers: selection, design, and operation, Second, edition. ed. Elsevier/BH, Amsterdam.

Hruska, P.J, Nellis, G.F., Klein S.A., 2016. Methodology of Modeling and Comparing the Use of Direct Air-Cooling for a Supercritical Carbon Dioxide Brayton Cycle and a Steam Rankine Cycle. The 5th International Symposium - Supercritical CO2 Power Cycles, San Antonio, Texas.

INPRO - International Project on Innovative Nuclear Reactors and Fuel Cycles, International Atomic Energy Agency, 2013. Challenges related to the use of liquid metal and molten salt coolants in advanced reactors: report of the Collaborative Project COOL of the International Project on Innovative Nuclear Reactors and Fuel Cycles.

Iverson, B.D., Conboy, T.M., Pasch, J.J., Kruizenga, A.M., 2013. Supercritical CO2 Brayton cycles for solar-thermal energy. Appl. Energy 111, 957–970. https://doi.org/10.1016/j.apenergy.2013.06.020.

Kim, E.S., Oh, C.H., Sherman, S., 2008. Simplified optimum sizing and cost analysis for compact heat exchanger in VHTR. Nucl. Eng. Des. 238, 2635–2647. https://doi.org/10.1016/j.nucengdes.2008.05.012.

Le Pierres, R, Southall, D., Osborne S., 2011. Impact of mechanical design issues on printed circuit heat exchangers. In: Proceedings of SCO2 Power Cycle Symposium, University of Colorado at Boulder - University Memorial Center, CO.

Li, X., Kong, W., Wang, Z., Chang, C., Bai, F., 2010. Thermal model and thermodynamic performance of molten salt cavity receiver. Renew. Energy 35, 981–988. https://doi.org/10.1016/j.renene.2009.11.017.

Liao, Z., Li, X., Xu, C., Chang, C., Wang, Z., 2014. Allowable flux density on a solar central receiver. Renew. Energy 62, 747–753. https://doi.org/10.1016/j.renene.2013.08.044.

Linares, J.I., Cantizano, A., Arenas, E., Moratilla, B.Y., Martín-Palacios, V., Batet, L., 2017. Recuperated versus single-recuperator re-compressed supercritical CO2 Brayton power cycles for DEMO fusion reactor based on dual coolant lithium lead blanket. Energy 140, 307–317. https://doi.org/10.1016/j.energy.2017.08.105.

Linares, J.I., Montes, M.J., Cantizano, A., Sánchez, C., 2020. A novel supercritical CO2 recompression Brayton power cycle for power tower concentrating solar plants. Appl. Energy 263, 114644. https://doi.org/10.1016/j.apenergy.2020.114644.

Medrano, M., Puente, D., Arenaza, E., Herrazti, B., Paule, A., Brañas, B., Orden, A., Domínguez, M., Stainsby, R., Maisonnier, D., Sardain, P., 2007. Power conversion cycles study for He-cooled reactor concepts for DEMO. Fusion Eng. Des. 82, 2689–2695. https://doi.org/10.1016/j.fusengdes.2007.04.041.

Mehos, M., Turchi, C., Vidal, J., Wagner, M., Ma, Z., Ho, C., Kolb, W., Andraka, C., Kruizenga, A., 2017. Concentrating Solar Power Gen3 Demonstration Roadmap (No. NREL/TP–5500-67464, 1338899). 10.2172/1338899.

Montes, M.J., Rovira, A., Martínez-Val, J.M., Ramos, A., 2012. Proposal of a fluid flow layout to improve the heat transfer in the active absorber surface of solar central cavity receivers. Appl. Therm. Eng. 35, 220–232. https://doi.org/10.1016/j.applthermaleng.2011.10.037.

Neises, T., Turchi, C., 2019. Supercritical carbon dioxide power cycle design and configuration optimization to minimize levelized cost of energy of molten salt power towers operating at 650 °C. Sol. Energy 181, 27–36. https://doi.org/10.1016/j.solener.2019.01.078.

NIST database https://webbook.nist.gov/chemistry/.

NREL https://www.nrel.gov/.

Sabharwall, P., Clark, D., Glazoff, M., Zheng, G., Sridharan, K., Anderson, M., 2014. Advanced heat exchanger development for molten salts. Nucl. Eng. Des. 280, 42–56. https://doi.org/10.1016/j.nucengdes.2014.09.026.

Samanes, J., García-Barberena, J., Zaversky, F., 2015. Modeling solar cavity receivers: a review and comparison of natural convection heat loss correlations. Energy Procedia 69, 543–552. https://doi.org/10.1016/j.egypro.2015.03.063.

Shiferaw, D., Carrero, J., 2016. Economic analysis of SCO2 cycles with PCHE Recuperator design optimisation. In: The 5th International Symposium - Supercritical CO2 Power Cycles, San Antonio, Texas.

Shouman, E.R.M., 2018. Economic Future of Concentrating Solar Power for Electricity Generation. In: Madejski, P. (Ed.), Thermal Power Plants - New Trends and Recent Developments. InTech. 10.5772/intechopen.74334.

Siegel, R., Howell, J.R., 2002. Thermal radiation heat transfer, 4th ed. Taylor & Francis, New York.

SolarPACES https://www.solarpaces.org/.

Southall, D., Le Pierres, R., Dewson, S.J., 2008. Design considerations for compact heat exchangers. International Congress on Advances in Nuclear Power Plants, American Nuclear Society. ICAPP'08 proceedings of the 2008 International congress on advances in nuclear power plants, California.

Srivastava, A.K., Vaidya, A.M., Maheshwari, N.K., Vijayan, P.K., 2013. Heat transfer and pressure drop characteristics of molten fluoride salt in circular pipe. Appl. Therm. Eng. 61, 198–205. https://doi.org/10.1016/j.applthermaleng.2013.07.051.

Stalin Maria Jebamalai, J., 2016. Receiver Design Methodology for Solar Tower Power Plants. Master Thesis. KTH School of Industrial Engineering and Management. Retrieved from http://urn.kb.se/resolve?urn=urn:nbn:se:kth:diva-192664.

Sun, H., Wang, J., Li, Z., Zhang, P., Su, X., 2018a. Corrosion behavior of 316SS and Ni-based alloys in a ternary NaCl-KCl-MgCl2 molten salt. Sol. Energy 171, 320–329. https://doi.org/10.1016/j.solener.2018.06.094.

Sun, X., Zhang, X., Christensen, R., Anderson, M., 2018. Compact Heat Exchanger Design and Testing for Advanced Reactors and Advanced Power Cycles (No. 13–5101, 1437159). 10.2172/1437159.

Turchi, C.S., Vidal, J., Bauer, M., 2018. Molten salt power towers operating at 600–650 °C: Salt selection and cost benefits. Sol. Energy 164, 38–46. https://doi.org/10.1016/j.solener.2018.01.063.

Wagner, M.J., Wendelin, T., 2018. SolarPILOT: A power tower solar field layout and characterization tool. Sol. Energy 171, 185–196. https://doi.org/10.1016/j.solener.2018.06.063.

Wang, K., He, Y.-L., Zhu, H.-H., 2017. Integration between supercritical CO2 Brayton cycles and molten salt solar power towers: A review and a comprehensive comparison of different cycle layouts. Appl. Energy 195, 819–836. https://doi.org/10.1016/j.apenergy.2017.03.099.

Yoon, S.-J., Sabharwall, P., Kim, E.-S., 2014. Numerical study on crossflow printed circuit heat exchanger for advanced small modular reactors. Int. J. Heat Mass Transf. 70, 250–263. https://doi.org/10.1016/j.ijheatmasstransfer.2013.10.079.

Zavoico, A.B., 2001. Solar Power Tower Design Basis Document, Revision 0 (No. SAND2001-2100, 786629). 10.2172/786629.